Title	Experimental investigation, numerical modelling and multi-objective optimisation of composite wind turbine blades
Author(s)	Fagan, Edward M.; Leen, Sean B.; de la Torre, Oscar; Jamie, Goggins
Publication Date	2017-05-24
Publication Information	Fagan, Edward M., Leen, Sean B., de la Torre, Oscar, & Goggins, Jamie. (2017). Experimental investigation, numerical modelling and multi-objective optimisation of composite wind turbine blades. Journal of Structural Integrity and Maintenance, 2(2), 109-119. doi: 10.1080/24705314.2017.1318043
Publisher	Taylor & Francis
Link to publisher's version	https://doi.org/10.1080/24705314.2017.1318043
Item record	http://hdl.handle.net/10379/15602
DOI	http://dx.doi.org/10.1080/24705314.2017.1318043

Experimental investigation, numerical modelling and multi-objective optimisation of composite wind turbine blades

Edward M Fagan[1,3,4], Sean B Leen[2,3,4], Oscar de la Torre[1,3,4], Jamie Goggins[1,3,4]

[1] *Civil Engineering, National University of Ireland, Galway, Ireland*

[2] *Mechanical Engineering, National University of Ireland, Galway, Ireland*

[3] *Ryan Institute, National University of Ireland, Galway, Ireland*

[4] *Marine and Renewable Energy Ireland (MaREI) Research Centre, Galway, Ireland*

Provide full correspondence details here including e-mail for the corresponding author

Corresponding author at: Civil Engineering, National University of Ireland, Galway, Ireland. Email address: Jamie.goggins@nuigalway.ie

Experimental investigation, numerical modelling and multi-objective optimisation of composite wind turbine blades

Static and modal testing of two blades from a 15 kW wind turbine is presented. The two blades are made from glass-fibre reinforced polypropylene, one of which has been reinforced with additional carbon-fibre plies. Static testing is performed with a Whiffle tree test rig to determine the structural response of the blades. Blade mass, deflections, strains and natural frequencies are reported. The following objectives are undertaken: (i) evaluate and compare the test results of the two wind turbine blade designs, (ii) use the results to validate finite element models of the blades and (iii) utilise the validated models in a design optimisation study. Parametric blade models are generated using the Python programming language and are based on manufacturing specifications for the blades. The models show good correspondence with the experimental results. The goal of the optimisation study is to maximise the stiffness and reduce the mass of the glass-fibre blade. A multi-objective genetic algorithm is used to determine the optimum laminate thicknesses along the length of the blades. The optimisation study produced a set of Pareto efficient blade designs with up to 17% improvement in stiffness or 30% reduction in mass for the glass-fibre blade design.

Keywords: wind turbine blade; structural testing; optimisation; finite element modelling; Non-dominated Sorting Genetic Algorithm-II (NSGA-II)

Introduction

Small-scale wind turbines are defined as having a rotor diameter from 0.5 to 10 m and typically have a standard power rating of between 1.4 and 16 kW (Tummala et al., 2016). The blades under investigation in this study are from a 15 kW turbine. This scale of device is aimed primarily at household power generation, focusing also on farms and small businesses. These turbines present a useful power source but their construction is dependent on two factors: (i) the initial costs and (ii) the unit cost per kWh produced. A major component in the initial and subsequent maintenance costs is the blades of the turbine. Hence, minimising the blade production costs is important for both initial

installation and for replacement due to the damage accumulated during operation. The efficiency of power generation is also of importance; from a mechanical perspective this represents the stiffness of the blades and, thereby, their energy conversion efficacy. The two blades tested in this study are constructed from glass-fibre reinforced polypropylene. One of the blades has additional carbon-fibre epoxy plies embedded in the spar caps to increase its stiffness. The addition of carbon-fibre dramatically increases the costs of production and also complicates the manufacturing process. Therefore, a balance is required between blade stiffness and the cost of materials. Other than the construction materials, the blades are aerodynamically identical and are interchangeable in the 15 kW turbine.

Structural testing is performed to demonstrate to a reasonable level of certainty that the wind turbine blade possesses the strength and service life for its original design (Det Norske Veritas, 2010). The strength and stiffness requirements for the blades ensure that they are strong enough not to break while also stiff enough to avoid striking the tower. The natural frequencies of the blades are of importance and should not coincide with the rotational frequency of the turbine to avoid resonance. Resonance will result in amplified vibrations leading to either tower strikes or fatigue failures of blades or other turbine components (Gurit, 2013). Static testing is often conducted before and after fatigue tests to provide a measure of the residual strength and stiffness of the structure due to the accumulation of damage (Lee & Park, 2016). Static tests are conducted by loading the blade at a number of discrete points along its length. Loading is generally applied via weights, cranes and clamps or hydraulic actuators (Zhou et al., 2014). The loads produce the equivalent bending moment distribution in the blade as from operational or extreme winds. Published studies present a wide range of scales of wind turbine blade tests: Chen (2017) investigated the local buckling and eventual

structural collapse of a 47 m long blade under combined bending and torsional loading, Yang et al. (2013) present 40 m blade static tests under flapwise loading, Overgaard et al. report on static tests (Overgaard, Lund & Thomsen, 2010) and computational modelling (Overgaard & Lund, 2010) of 25 m long blades and Larwood and Musial (Larwood & Musial, 2000) have shown results from static, fatigue and modal testing of 12 m blades. From a review of small scale wind turbines (Tummala et al., 2016) only one study was cited for the design and testing of a turbine blade similar to the scale presented here (Habali & Saleh, 2000). One point noted by the review author was a lack of research on the optimisation of the blade design for manufacturing purposes for this scale of blade. The majority of research instead focused on the aerodynamic performance characteristics such as varying tip speed ratio, rotor speed and pitch angle.

Numerical optimisation techniques provide a powerful tool for designers to assess the myriad structural and aerodynamic variables related to blade design. A number of researchers have demonstrated the effectiveness of these techniques for the design of composite wind turbine blades. Jureczko et al. (2005) presented a modified genetic algorithm for the multi-criteria optimisation of blade structures, resulting in significant mass savings. Chen et al. (2013) demonstrated the use of a particle swarm algorithm for blade mass reduction. Lund and Stegmann (2005) developed an optimisation procedure focused on blade stiffness or eigenfrequencies, using a gradient-based technique. Paluch et al. (2008) used a genetic algorithm to investigate the effect of ply thickness and fibre orientation on blade mass for composite structures. The technique used in the current study is the nondominated sorting genetic algorithm (NSGA-II) developed by Deb et al. (2002) for multi-objective optimisations. This approach has been modified to use finite element models, which have been calibrated against experimental static tests, to assess the objective functions in the study. The

parametric finite element blade models are generated from geometric and manufacturing data. The variables under consideration are the thickness distribution of the laminates and the location of discrete changes in thickness (ply drops) along the length of the blade. The aim for the study is to find the optimum structural design for a glass fibre blade to achieve the maximum stiffness with minimal increase in mass.

[Figure 1 near here]

Methods

Experimental testing

Structural testing of wind turbine blades involves applying an equivalent mechanical load to match the aerodynamic loading the blade experiences. The greater the number of load points the more accurately the bending moment distribution is reproduced. Figure 1 shows the Whiffle tree rig used in the experiments. The Whiffle tree splits the crane load between eight separate loading points. The eight points each apply a percentage of the total load to the surface of the blade via bars. This distribution has been determined from the operating conditions of the wind turbine. Figure 1 highlights some of the features of the test setup including, the load cell which is connected between the Whiffle tree rig and the crane, several of the strain gauge locations on the compressive side of the blade and the locations of several of the loading points. Figure 2 (a) shows the locations of the load points and the percentage of the total load applied at each. As can be seen in Figure 3, the root connection of the blade is slanted at approximately 50° to the length of the blade. For all of the figures in this paper the starting point of the root region is considered the zero point lengthwise. Hence, the negative value for the first load bar in Figure 2 (a). Figure 2 (b) shows the resulting bending moment distribution over the blade.

The blades were instrumented with a combination of $120 \pm 0.4\%$ Ω (model Micro Measurements EA-06-060RZ-120) linear electrical resistance strain gauges and $120 \pm 0.5\%$ Ω (model Tokyo Sokki Kenkyujo Co. Ltd. FLA-6-11-3LT) linear electrical resistance strain gauges. The strain gauges were orientated along the length of the blade. Three draw-wire displacement sensors (model Micro-Epsilon WDS-500-P60-CR-P) with a measuring range of 500 mm (linearity $\pm 0.1\%$ FSO) and one draw-wire displacement sensor (model Micro-Epsilon WDS-1000-P60-BH-PB) with a measuring range of 1000 mm (linearity $\pm 0.1\%$ FSO) were used to measure the blade deflection. The locations of the strain gauges and stringpots are provided in Table 1. The load applied through the crane to the Whiffle tree was measured with a Sensotec 50000 lbs/222.4 kN load cell (model 41/0573-01, linearity $\pm 0.1\%$ full scale).

[Figure 2 near here]

Additionally, modal tests were conducted using an impact hammer and a number of accelerometers. The modal tests were used to determine the natural frequencies for the first three flapwise bending modes of the blades. The tests required a Dytran model 5805A impulse sledge hammer with a one pound head (sensitivity 1 mV/lbf) and four accelerometers (model ENDEVCO 752A12). Table 1 also shows the locations of the accelerometers and the location of impact hammer strikes on the blade. A Leica C10 ScanStation laser scanner was used to scan the blades before and after applying the static load. The scanner has a resolution of one point every 20 cm at the lowest level and one point every 10 cm at the medium level of operation, at a range of 100 m. At an average distance of 3 m, the low resolution scans resulted in a point measurement every 6 mm and for medium resolution a point every 3 mm. The mass of the blades was measured before each static test using a weighing scales (linearity 0.25% FSO) and harness.

During the test the carbon-fibre reinforced blade (CFPP) was loaded to approximately 1 kN while the glass-fibre blade (GFPP) was loaded to approximately 500 N. The difference in total loads was due to the upper limits on the stringpots being reached in the case of the GFPP blade. As an additional strength check, both blades were also loaded to approximately 1.3 times the full load with the stringpots removed, while still recording the blade strains. The results reported in Section 3 state the total crane load as appropriate.

The key measurements sought in the experiment were the distribution of strain along the blades, the blade deflections and the natural frequencies for comparison with the finite element (FE) models. The strain gauges were located along the centre line of the spar cap on the compression side of the blade. From the initial FE models the highest strains in the blades were found on the compression side, this also helped to avoid the load application bars from damaging the gauges when installing the rig.

The blades were constructed primarily from laminates made from glass-fibre polypropylene, with carbon-fibre epoxy used in the spar caps of the reinforced blade. Two types of glass-fibre polypropylene were used, Twintex and Plytron. Table 2 shows the material properties for unidirectional plies of typical Twintex, Plytron (Long, 2005) and carbon-fibre epoxy.

[Table 1 near here]

Structurally, the blades consist of three main sections: the spar caps, the shear web and the outer aerodynamic skin. The spar caps and shear web essentially form an I-beam which acts as the main structural component of the blade. Layers of unidirectional Plytron plies orientated along the length of the blade make up the spar caps and the shear web is constructed from biaxial 0°/90° plies. The aerodynamic skin is made from biaxial layers of Twintex orientated at ±45° to the longitudinal axis of the blade. The

shear web is located at approximately 30% of the chord length for the entire length of the blade. Due to the proprietary nature of the blade a simplified version of the blade layups is presented in Figure 3. The variables $x_1 - x_{29}$ refer to the design optimisation methodology, further discussion of which can be found in Section 2.3 below.

The geometry of the blade is described primarily by the distribution of the chord length and aerodynamic twist angle (Table 3). NACA 4415 airfoils define the shape of the blade, with a transition to a rectangular section at the root.

[Table 2 and Figure 3 near here]

Finite element modelling

The finite element package used in this work is Abaqus Standard (ABAQUS, 2016). A number of research groups have shown the applicability of a shell-based approach to modelling composite wind turbine blades (Yang et al., 2013; Kong et al., 2005; Jensen et al., 2006). A composite layup can be applied to shell elements in the FE program, allowing quick and accurate modelling of the behaviour of the blades. Low computational cost and fast turnaround are required since a large number of models must be analysed during the optimisation study; typically thousands before the optimal set of solutions is determined.

The FE models are generated using a Python code developed in-house and previously used to model concept tidal turbine blades (Fagan et al., 2016a) and validated against 13 m long wind turbine blade tests (Fagan et al., 2016b). The code requires geometric, material and structural input data such as that outlined in the previous section (and summarised in Table 4). Once the required inputs have been set, the code automatically generates the full FE model, performs the analysis and post-processes the results for evaluation of the optimisation objectives.

[Table 3 and 4 near here]

The aerodynamic lift and drag forces on a wind turbine blade are resolved into the forces perpendicular (flapwise) and parallel (edgewise) to the rotor plane. The edgewise forces cause the torque on the turbine and the flapwise forces the thrust. The flapwise loads are generally an order of magnitude higher than the edgewise loads and are more critical during static strength tests. The current set up with the Whiffle tree rig is restricted to testing the blade in the flapwise direction. Further testing is recommended to account for the edgewise loading and additional high-cycle fatigue testing to fully analyse the wind turbine blade structural performance.

In order to apply the out of plane loading to the blade, eight partitions matching the loading locations (from Figure 2 (a)) are created. The width of the partitions matches the load application bars and the same percentage of the load applied via the Whiffle tree rig is applied in the models.

The loads are applied to the blade using a structural distributed coupling constraint in Abaqus. The nodes in the section where the load is applied are constrained to a reference point. Point loads are applied to the reference points and distributed to the section via the coupling. The root of the blade is constrained in all six degrees of freedom. A schematic of the loading and boundary conditions on a typical blade model is shown in Figure 4.

[Figure 4 near here]

The FE models use S4R 4-noded, doubly curved, reduced integration, linear shell elements. A mesh convergence study was performed in order to minimise the computational expense of each analysis. The results of the convergence study are shown in Figure 5. The first three bending mode natural frequencies were used to determine mesh convergence. At approximately 30,000 nodes the solution had converged and this was the model size used in the analysis. The mesh seeding resulted in elements

measuring approximately 14 mm per side. Further refinement was employed for elements in the spar caps and shear web, where the average element dimensions were reduced to approximately 2 mm by 12 mm.

[Figure 5 near here]

Multi-objective design optimisation

The optimisation task is focused on maximising the stiffness of the glass-fibre blade while also minimising the resultant blade mass. The NSGA-II multi-objective algorithm was used to determine the Pareto efficient set of solutions for the design problem. The operation of the NSGA-II algorithm can be found in detail in (Deb et al., 2002).

Section 2.3.1 outlines in detail the method of encoding the blade structural design into a vector of design variables (or chromosome) for the problem. Section 2.3.2 provides an explanation for the genetic algorithm operators applied in the analysis, these include: the two-point crossover method, mutation of the design variables and the repair function. Section 2.3.3 describes the objective functions used to evaluate the fitness of each potential blade design and Section 2.3.4 summarises the operating parameters used in the final optimisation.

Genetic encoding

In the present study, the thickness distribution of the laminates along the length of the blade was investigated, while the blade geometry and material properties remained constant. Each blade design is encoded in a design vector, x, of twenty-nine variables. The variables control the thickness of the laminates in the spar caps, outer shell and shear web and the location of the four ply drops in the blade. The four ply drops split the blade into five distinct regions. Figure 3 shows a cross-section through a blade, indicating the various regions and the design variables that control the laminate

thicknesses. The genetic algorithm controls the layups of the blade up to 3750 mm from the zero point on the blade, after which a standard layup for the tip region is applied.

[Table 5 near here]

The design variables are shown in Table 5 alongside their respective minimum and maximum allowable values. The first five variables define the number of unidirectional plies in the spar caps for each blade section. The next five define the number of biaxial (45°/135° woven plies) in the outer aerodynamic skin. A minimum of 2 was employed to ensure that any unidirectional spar cap plies would be embedded between biaxial layers. The setup of the code is such that additional skin plies (controlled by variables x_6-x_{10}) are added on top of the UD layers. This has the effect of pushing the UD layers further from the surface of the blade. The next five (x_{11}-x_{15}) design variables add further biaxial layers to the inner surface of the cavity in the blade formed between the trailing edge and the shear web. Figure 3 shows how these plies are added to the trailing edge, spar caps and webs on the inner surface of the blade. The next five design variables (x_{16}-x_{20}) reinforce the blade in a similar way, but for the leading edge region. The variables x_{21}-x_{25} control the thickness of the 0°/90° layers in the shear web for each region and the final four variables control the locations of the ply drops. The Python code uses a polynomial curve fit of the chord and twist data from Table 3 to ensure the blade geometry remains smooth and constant between different blade designs.

Before the FE analysis is performed for each blade design, an initial check of the thickness of the laminates all along the blade is performed. This is required to avoid the non-physical overlap of the top and bottom spar caps which is possible from the random generation of design vectors. If the laminates are found to overlap then the repair function is called, this is discussed in detail in the following section.

Crossover, mutation and repair

In order to promote genetic diversity in the new population, crossover and mutation operators are applied within the genetic algorithm. Crossover is a process whereby two parent individuals are randomly chosen from the population and their design vectors are combined to create a pair of new individuals. After the new individuals are created each variable in their design vectors is exposed to a chance of randomly mutating to a value within its upper and lower limits. Repair functions are used to fix the design vectors of individuals that are infeasible, through either their random generation at the beginning of the optimisation, mutation or crossover processes.

[Figure 6 near here]

For this study, a two point crossover procedure was applied. Single point crossover is a more common approach; however, it proved unsuitable for use with the design vector's structure. The last four design variables, those that define the ply drop locations, almost invariable require repair when they have been involved in a crossover procedure. Since repairing them often meant that little information from either parent design was retained, it was decided to exclude the last four variables from the crossover procedure. In order to avoid introducing any bias into how the parent individuals are crossed-over, a two-point crossover method was devised. Two split points were randomly generated in the design vectors (Figure 6), resulting in three pairs of child individuals. One of these pairs is randomly selected for inclusion in the newly generated population.

As previously mentioned, each variable in the newly generated individuals is exposed to the chance of a random mutation. For the first twenty-five variables this simply involves changing the value to a randomly generated integer between their respective maximum and minimum allowable limits. The remaining four design

variables can mutate between their adjacent ply drop locations. For example, the second ply drop location can vary between the first location and third. A minimum clearance of 100 mm is enforced between ply drop locations. This means the minimum location for the first ply drop is 100 mm from the zero location and the maximum location of the last drop is at 3650 mm.

In order to ensure that the genetic algorithm does not generate a blade with overlapping spar caps, the thickness of the laminates is compared to the available space inside the blade along its length after the model is generated. A polynomial curve fit of the blade thickness distribution is compared to the discrete laminate thicknesses between ply drops. If the thickness of the laminates exceeds the available space (less a cavity required for inflating the bagging during the curing procedure) then the design variables in that region are reduced until the constraint is satisfied.

The order in which the repair function reduces the design variables is: variables related to the outer aerodynamic skin (x_6-x_{10}), then the variables related to the inner leading edge or trailing edge laminates (x_{11}-x_{20}) and finally the spar cap plies (x_1-x_5). The order in which plies are removed introduces some bias into the algorithm, as it favours reinforcement due to the inner leading and trailing edge laminates over the outer skin laminates. This was chosen to direct analysis towards spar cap plies located in the outermost plies of the blade, increasing the bending stiffness of the I-beam and, hence, improving the overall stiffness of the blade. This bias in the repair function was unavoidable for the current encoding method and future work will investigate its effect on the optimisation.

The repair function was called with some frequency in the initial stages of the analysis since the initial population is formed from randomly generated design

variables. The function was then required later in the optimisation due to the mutation and crossover procedures.

Objective functions

Multi-objective optimisations require the definition of two or more objective functions to determine the fitness of each individual relative to the population. The first objective function is the tip deflection of the blade; by minimising the tip deflection the overall blade stiffness is maximised. An overly flexible blade implies inefficient energy transfer, can result in significant changes to the aerodynamics of the turbine and can result in the blade tip striking the tower in extreme cases. The second objective function is the mass of the blade. Minimising the blade mass can help reduce the material and manufacturing costs. The optimisation can be represented as:

$$\min_{x \in D} f\big(g_1(x), g_2(x)\big)$$

where,

$$g_1(x) = \delta_{tip}(x)$$

$$g_2(x) = M(x)$$

where $\delta_{tip}(x)$ is the tip deflection of the blade, $M(x)$ is the mass of the blade, x is the vector of design variables and D represents the design space containing all possible solutions.

Operating parameters

The parameters for the genetic algorithm include:

- A total of 20 individuals in the population

- A total of 150 generations

- Pairs of individuals had a 90% chance of crossover occurring

- A 3% chance of mutation for each design variable.

Results and Discussion

Experimental results and FE comparison

Blade mass and centre of gravity

Figure 7 shows the comparison between the masses of the test blades and FE models. A difference of 6.5% and 6.7% exists between test blade and model for the GFPP and CFPP blades respectively. The causes of the discrepancies are likely due to, (i) variations in the fibre volume content of the glass-fibre material in different batches, (ii) an overlap between adjacent layers of biaxial material which is not included in the models and (iii) non-structural material such as bagging remaining in the blades. The blades were weighed after instrumentation, therefore their mass values include the strain gauges and lead wires.

The centres of gravity (COGs) for the two blades were also measured and compared to the FE models. The results are reported in Figure 8. The locations, both chord-wise and along the length of the blade, of the COGs for the GFPP blade are quite close in value. The results for the CFPP blade are somewhat less favourable, with the FE model predicting the COG to be approximately 160 mm further along the blade. While the difference in mass between the model and actual blades is quite low, the difference in COG indicates that the distribution of material in the FE model is to some degree unrepresentative of the actual blade.

[Figure 7 and 8 near here]

Blade deflections

Figure 9 shows the results of the static tests on the two blades along with the associated FE model results. The blade deflections are shown for the same load applied to both blades (approximately 500 N). During the test two LVDT (linear variable differential transformer) displacement sensors were used to monitor displacement of the support plate the blade was mounted to. A small vertical displacement of the plate was noted during the tests and the blade deflection results were corrected appropriately. The significant increase in stiffness due to the addition of the carbon-fibre plies is evident with a reduction in tip deflection of approximately 71%.

[Figure 9 near here]

The tip deflections (normalised by the blade lengths) from experiments and FE are reported in Figure 10. The model of the GFPP blade showed good correspondence with the test results, over predicting the experimental value by approximately 6% (41 mm). The model of the CFPP blade was less accurate, under predicting the test by approximately 24% (49 mm).

After the initial static test the two blades were tested to approximately 1.3 times the initial load, 640 N for the GFPP blade and approximately 1325 N for the CFPP blade. The laser scanner was employed to determine the blade deflections, since the deflections were past the limits of the stringpots available. Figure 11 shows the point cloud generated by the laser scanner. The scanner performed a low and medium resolution scan at the initial unloaded blade position, then another low resolution scan at the loaded position. Overlaying the three scans allows for measurements of blade deflection to be taken. Table 6 shows the measurements of the tip deflection for the GFPP blade at 640 N. The y-direction is aligned with the blade, positive towards the tip, and the x-direction is perpendicular and positive into the image.

[Figure 10 and 11 near here]

The tip deflection in the x- and y-direction from FE model is also shown in Table 6 for comparison. At the high load level, the y-deflection is significantly different from the FE results. Due to the deflection of the blade/rig it was found that the direction of loading on the blade was not vertical in this extreme example. The distributed loading constraint in the FE models only applied load in the vertical direction, indicating a source of error between models and experiments for high tip deflection cases. An alternative loading method for the FE models is to apply rigid beam elements which will reflect the changing directionality of the load towards the tip of the blade. However, due to the complexity of the Whiffle tree rig this modelling effort is left to a future study.

[Table 6 near here]

Blade natural frequencies

Figure 12 presents the first three bending mode natural frequencies from the experiments and the FE models. The natural frequencies of the CFPP blade were expected to be higher in value than the GFPP blade due to the increased stiffness, which is reflected in both experimental and FE results. The first two natural frequencies show good agreement for the GFPP blade, however the difference in the third natural frequency indicates some discrepancy between models and physical blades. Similarly, the predictions for the first two frequencies for the CFPP blade are quite close, with the third value showing disagreement.

[Figure 12 near here]

Blade strains

The strain distribution, at a load of 500 N, from both experiments and FE is plotted in

Figure 13. The results for the CFPP blade are quite close, however, the FE model consistently under-predicts the strain (as expected by the under prediction of blade deflection). The GFPP results are also quite close, however, a major discrepancy between the results is evident from approximately 0.35 L to 0.7 L. The higher strain predictions also match the over prediction of deflection by the FE model. Peaks are evident in the FE results where ply drops occur.

[Figure 13 and Figure 14 near here]

Figure 14 shows the strain along the length of the CFPP blade at loads of 300 N, 500 N and 965 N. The strain was found to increase linearly with load at least as far as 965 N. The strain is highest between approximately 0.3 L and 0.45 L along the blade. The laminates in the root region experience the highest bending moment (from Figure 2 (b)), however, they are also the thickest laminates in the blade, resulting in the reduction in the strain from 0.3 L towards the root. From Figure 13 it can be seen that at the highest strained location, 0.3 L, the strain in the GFPP blade is approximately 3.9 times that in the CFPP blade for the same load.

Figure 15 shows the longitudinal stress in each ply through the thickness of the laminate at the location of the second strain gauge (0.2 L along the blade) at 500 N, from the FE model. The stresses have been resolved into the ply coordinate system, i.e. the plot shows the magnitude of the fibre-direction stress in each ply of the laminate.

[Figure 15 near here]

Optimisation results

Figure 16 presents the results from the multi-objective optimisation. The majority of the results span blade masses from approximately 8 kg to 35 kg and tip deflections from approximately 0.16 L to 0.4 L. Figure 17 (a) and (b) show the development of the two objective function values for each member of the population through each generation.

From generation 140, Figure 17 (b) shows that the algorithm found several solutions with a low mass but very high tip deflection (approximately 0.9 L); the results in Figure 16 have been truncated to provide greater clarity for the range of viable blade designs.

The initial population was randomly generated by the algorithm and lead to the large spread of high-mass and high-deflection individuals in the top right quadrant of Figure 16. As the search proceeded, the average value of the blade mass for each population decreased as the algorithm converged to the Pareto optimum solution set for the problem. The general trend for the Pareto set is that as blade mass decreases the tip deflection increases, i.e. the blades become more flexible. This trend is also evident in the objective function results in Figure 17 (a) and (b). As the average mass of the blades for the population in each generation decreases the average value of the tip deflection for the population increases.

[Figure 16 and 17 near here]

Table 7 (in Appendix A) shows a selection from this Pareto efficient set of solutions. Solutions 14 and 20 from this set are now investigated in detail. The blade deflection for solution 20 is plotted alongside the experimental and FE results in Figure 9. This blade design showed a 17.2% decrease in tip deflection from the experimental GFPP blade, with a 29% increase in mass. Solution 14 represents a blade design with a 0.3% increase in tip deflection from the experimental blade, however, it shows a 31.4% decrease in blade mass. From the results of the search, it is apparent that there is a limit to the improvement in blade stiffness, within the constraints of the current layup options and glass-fibre materials, at approximately 0.157 L; however, there is a significant opportunity for reducing the mass of the blades while retaining reasonable tip deflections.

[Figure 18 near here]

A comparison between the thickness of the laminates along the length of the GFPP, CFPP and solution 20 blades is shown in Figure 18. The three blades show the general trend of decreasing laminate thickness along their lengths. The GFPP blade shows increases at two locations, due to overlaps in the biaxial layers. Both of the experimental blades were designed with the majority of their ply drops in the first half of the blade length (four from six for the CFPP blade and five from nine for the GFPP blade); however, the optimum blade resulted in all of the available ply drops in the outer half of the blade. This result was also found in all of the Pareto efficient solutions in Table 7. Since ply drops generally result in stress concentrations this is considered an improvement in the blade design. Three of the five ply drops in solution 20 occur at a length greater than 0.75 L, where the strains are among the lowest values along the length of the blade, as evidenced in Figure 13.

Figure 19 shows the first three natural frequencies for blades 14 and 20. The three natural frequencies have not showed significant change from the FE model of the original GFPP blade.

[Figure 19 near here]

All computations were conducted on an Intel core i7 desktop computer with 8 CPUs and 16 GB RAM. Each analysis took approximately 2.5 minutes to run, including model generation and post-processing. The total duration of the optimisation search was approximately 108 hours. A total of 2527 models were generated and assessed for the study.

Conclusion

This paper presents the results of static and modal tests on two blade designs for a 15 kW wind turbine. The two blades are constructed from glass-fibre polypropylene (GFPP) and one has additional carbon-fibre epoxy reinforcement (CFPP). Finite

element (FE) modelling is conducted and the test results used to calibrate the models. A multi-objective optimisation was then performed with the aim of improving the stiffness and reducing the mass of the glass-fibre blade design. The following represent the most significant findings in the paper:

- The GFPP FE model showed good correspondence with the test results. The FE model was within 6.5% of the blade mass, 5.9% of the tip deflection and showed a relatively close comparison with the first three natural frequencies and the blade strains.

- The FE model of the CFPP blade was somewhat less accurate. The mass results were within 6.7% and the tip deflection within 23.7%. The natural frequency results were relatively close, as were the strain results along the length of the blade.

- Results from a laser scan of the blades at high loading indicated deflections in the blades not predicted by the FE models. The directionality of the loading from the test rig at high blade deflections and the applicability of the structural distributed loading constraint in the FE models will be further investigated as two sources of error in the methodology.

- The optimisation produced a set of Pareto efficient blade designs that showed up to 17% improvement in blade stiffness for a solely glass-fibre polypropylene blade.

- The optimal solution set also found that for a blade with similar stiffness to the GFPP test blade up to 30% savings in mass could be made.

The optimised glass-fibre blade designs represent a compromise on stiffness from the carbon-fibre reinforced blade but a significant improvement on the original

glass-fibre design. Future work will expand the scope of the design variables to include the width of the spar caps, the location of the shear web and combinations of FRP materials in the multi-objective optimisation.

References

ABAQUS. (2016). Abaqus Documentation. Providence, RI, USA: Dassault Systemes.

Chen, J., Wang, Q., Shen, W. Z., Pang, X., Li, S., & Guo, X. (2013). Structural optimization study of composite wind turbine blade. *Materials & Design*, *46*, 247–255. http://doi.org/10.1016/j.matdes.2012.10.036

Chen, X. (2017). Experimental investigation on structural collapse of a large composite wind turbine blade under combined bending and torsion. *Composite Structures*, *160*, 435–445. http://doi.org/10.1016/j.compstruct.2016.10.086

Deb, K., Pratap, A., Agarwal, S., & Meyarivan, T. (2002). A fast and elitist multiobjective genetic algorithm: NSGA-II. *IEEE Transactions on Evolutionary Computation*, *6*(2), 182–197. http://doi.org/10.1109/4235.996017

Det Norske Veritas. (2010). Design and Manufacture of Wind Turbine Blades, Offshore and Onshore Wind Turbines. *DNV Standard, DNV-DS-J102*, (OCTOBER).

Fagan, E. M., Flanagan, M., Leen, S. B., Flanagan, T., Doyle, A., & Goggins, J. (2016a). Physical Experimental Static Testing and Structural Design Optimisation for a Composite Wind Turbine Blade. *Composite Structures*, *164*, 90–103. http://doi.org/10.1016/j.compstruct.2016.12.037

Fagan, E. M., Kennedy, C. R., Leen, S. B., & Goggins, J. (2016b). Damage mechanics based design methodology for tidal current turbine composite blades. *Renewable Energy*, *97*, 358–372. http://doi.org/10.1016/j.renene.2016.05.093

Gurit. (2013). Wind Turbine Blade Structural Engineering. *Wind Energy Handbook*, 16.

Habali, S. M., & Saleh, I. A. (2000). Local design, testing and manufacturing of small mixed airfoil wind turbine blades of glass fiber reinforced plastics. *Energy Conversion and Management*, *41*(3), 281–298. http://doi.org/10.1016/S0196-8904(99)00104-1

Jensen, F. M., Falzon, B. G., Ankersen, J., & Stang, H. (2006). Structural testing and

numerical simulation of a 34m composite wind turbine blade. *Composite Structures*, *76*(1–2), 52–61. http://doi.org/10.1016/j.compstruct.2006.06.008

Jureczko, M., Pawlak, M., & Mężyk, A. (2005). Optimisation of wind turbine blades. *Journal of Materials Processing Technology*, *167*(2–3), 463–471. http://doi.org/10.1016/j.jmatprotec.2005.06.055

Kong, C., Bang, J., & Sugiyama, Y. (2005). Structural investigation of composite wind turbine blade considering various load cases and fatigue life. *Energy*, *30*(11–12), 2101–2114. http://doi.org/10.1016/j.energy.2004.08.016

Larwood, S. M., & Musial, W. (2000). Comprehensive Testing of Nedwind l2-meter Wind Turbine Blades at NREL. *19th American Society of Mechanical Engineers (ASME) Wind Energy Symposium*, (C), 297–305.

Lee, H. G., & Park, J. (2016). Static test until structural collapse after fatigue testing of a full-scale wind turbine blade. *Composite Structures*, *136*, 251–257. http://doi.org/10.1016/j.compstruct.2015.10.007

Long, A. C. (2005). *Design and manufacture of textile composites* (first). Cambridge, UK: Woodhead Publishing Limited.

Lund, E., & Stegmann, J. (2005). On structural optimization of composite shell structures using a discrete constitutive parametrization. *Wind Energy*, *8*(1), 109–124. http://doi.org/10.1002/we.132

Overgaard, L. C. T., & Lund, E. (2010). Structural collapse of a wind turbine blade. Part B: Progressive interlaminar failure models. *Composites Part A: Applied Science and Manufacturing*, *41*(2), 271–283. http://doi.org/10.1016/j.compositesa.2009.10.012

Overgaard, L. C. T., Lund, E., & Thomsen, O. T. (2010). Structural collapse of a wind turbine blade. Part A: Static test and equivalent single layered models. *Composites Part A: Applied Science and Manufacturing*, *41*(2), 257–270. http://doi.org/10.1016/j.compositesa.2009.10.011

Paluch, B., Grédiac, M., & Faye, A. (2008). Combining a finite element programme and a genetic algorithm to optimize composite structures with variable thickness. *Composite Structures*, *83*(3), 284–294. http://doi.org/10.1016/j.compstruct.2007.04.023

Tummala, A., Velamati, R. K., Sinha, D. K., Indraja, V., & Krishna, V. H. (2016). A review on small scale wind turbines. *Renewable and Sustainable Energy Reviews*, *56*, 1351–1371. http://doi.org/10.1016/j.rser.2015.12.027

Yang, J., Peng, C., Xiao, J., Zeng, J., Xing, S., Jin, J., & Deng, H. (2013). Structural investigation of composite wind turbine blade considering structural collapse in full-scale static tests. *Composite Structures*, *97*, 15–29. http://doi.org/10.1016/j.compstruct.2012.10.055

Zhou, H. F., Dou, H. Y., Qin, L. Z., Chen, Y., Ni, Y. Q., & Ko, J. M. (2014). A review of full-scale structural testing of wind turbine blades. *Renewable and Sustainable Energy Reviews*, *33*, 177–187. http://doi.org/10.1016/j.rser.2014.01.087

Appendix A

A selection of the results from the Pareto efficient set of designs found by the multi-objective genetic algorithm are shown in Table 7. The twenty blade designs are listed with both their objective function values, the generation they were first found and their 29 design variables.

[Table 7 near here]

List of Tables and Table Captions

Table 1. Normalised blade locations of the strain gauges, accelerometers, stringpots and the impact hammer strikes.

Stain Gauges	CFPP	GFPP
SG1	0.09	0.09
SG2	0.20	0.20
SG3	0.33	0.32
SG4	0.48	0.48
SG5	0.52	0.52
SG6	0.61	0.61
SG7	0.73	0.74
Stringpots		
SP1	0.27	0.27
SP2	0.39	0.39
SP3	0.61	0.61
SP4	0.72	0.72
SP5	0.89	0.89
Accelerometers		
A1	0.20	0.20
A2	0.33	0.32
A3	0.66	0.72
A4	0.88	0.88
Impact Hammer		
L1	0.81	0.81
L2	0.56	0.57
L3	0.30	0.30

Table 2. Unidirectional material properties of the composite plies used in the blade models (Long, 2005).

	E_1 (GPa)	E_2 (GPa)	G_{12} (GPa)	v_{12}
Twintex	21.5	6.0	1.00	0.20
Plytron	28.0	3.5	1.39	0.35
Carbon-Fibre Epoxy	104.6	6.9	3.67	0.32

Table 3. The blade geometry is described by the distribution of chord length and aerodynamic twist angle.

Location (x/L)	Chord (c/L)	Twist (°)
-0.10	0.109	23.5
-0.05	0.109	23.5
0.00	0.107	21.9
0.05	0.094	20.2
0.10	0.083	18.6
0.15	0.074	17.0
0.20	0.067	15.5
0.25	0.060	14.0
0.30	0.056	12.6
0.35	0.052	11.2
0.40	0.049	9.9
0.45	0.047	8.7
0.50	0.045	7.5
0.55	0.045	6.4
0.60	0.044	5.3
0.65	0.044	4.3
0.70	0.044	3.4
0.75	0.044	2.5
0.80	0.043	1.7
0.85	0.043	0.9
0.90	0.042	0.2
0.95	0.040	-0.5
1.00	0.000	-1.1

Table 4. Input data for blade finite element models.

Input Variable	Units
Chord length	mm
Aerodynamic twist	°
Location of leading edge	mm
Material properties	GPa
Layups for each blade section	-
Flapwise loading	N
Airfoil designations	NACA-xxxx
Spar cap width and location	mm, % Chord
Shear web location	% Chord

Table 5. Design variables, their limits and optimum values. TE = trailing edge laminates, LE = leading edge laminates.

Name	Description	Min	Max
x_1	Spar 1	1	20
x_2	Spar 2	1	20
x_3	Spar 3	1	20
x_4	Spar 4	1	20
x_5	Spar 5	1	20
x_6	Skin 1	2	20
x_7	Skin 2	2	20
x_8	Skin 3	2	20
x_9	Skin 4	2	20
x_{10}	Skin 5	2	20
x_{11}	TE 1	0	20
x_{12}	TE 2	0	20
x_{13}	TE 3	0	20
x_{14}	TE 4	0	20
x_{15}	TE 5	0	20
x_{16}	LE 1	0	20
x_{17}	LE 2	0	20
x_{18}	LE 3	0	20
x_{19}	LE 4	0	20
x_{20}	LE 5	0	20
x_{21}	Web 1	1	20
x_{22}	Web 2	1	20
x_{23}	Web 3	1	20
x_{24}	Web 4	1	20
x_{25}	Web 5	1	20
x_{26}	Ply Drop 1	100	x_{27}-100
x_{27}	Ply Drop 2	x_{26}+100	x_{28}-100
x_{28}	Ply Drop 3	x_{27}+100	x_{29}-100
x_{29}	Ply Drop 4	x_{28}+100	3650

Table 6. Tip deflections from laser scans (1325 N and 640 N applied load for the CFPP and GFPP blades respectively).

	x (mm)	y (mm)
GFPP - Experiment	55	-223
GFPP - FE	165	-15
CFPP - Experiment	100	-117
CFPP - FE	89	-7

Table 7. Selected results from the Pareto efficient set of designs.

	$M(x)$ (kg)	$\delta_{tip}(x)/L$	Gen	x_1	x_2	x_3	x_4	x_5	x_6	x_7	x_8	x_9	x_{10}	x_{11}	x_{12}
1	8.2	0.891	140	1	16	16	5	2	2	2	2	2	8	0	1
2	9.0	0.376	141	6	18	16	15	2	2	2	2	2	2	0	1
3	9.1	0.306	128	10	16	16	9	2	4	2	2	6	2	5	1
4	9.6	0.296	150	10	16	16	17	2	2	2	2	2	2	0	1
5	10.0	0.274	114	10	16	16	17	15	9	2	2	2	2	0	1
6	10.4	0.265	136	10	16	16	17	2	2	2	2	2	2	0	1
7	10.6	0.224	149	20	20	16	5	2	2	2	2	2	2	0	1
8	10.7	0.220	133	20	10	16	7	2	2	2	2	2	2	0	1
9	11.0	0.211	150	20	20	16	5	2	2	2	2	2	2	0	1
10	11.3	0.207	146	20	20	16	5	2	2	2	2	2	2	0	1
11	11.7	0.201	149	20	18	16	17	2	2	2	2	2	2	0	1
12	12.0	0.195	135	20	20	16	5	2	6	2	2	2	2	0	1
13	12.3	0.194	150	20	20	16	5	2	2	2	2	2	2	0	4
14	**12.7**	**0.189**	**144**	**20**	**20**	**16**	**5**	**2**	**2**	**2**	**2**	**2**	**2**	**0**	**1**
15	13.0	0.183	149	20	20	16	5	2	2	2	2	2	2	0	1
16	16.3	0.169	150	20	20	16	17	2	2	2	2	2	2	0	1
17	19.6	0.167	144	20	1	20	20	2	2	2	2	2	2	4	1
18	22.1	0.159	150	20	20	16	17	2	2	2	2	2	2	4	1
19	22.2	0.158	145	20	20	16	17	2	2	2	2	2	2	4	1
20	**23.9**	**0.157**	**50**	**20**	**18**	**16**	**17**	**17**	**2**	**2**	**2**	**2**	**2**	**4**	**4**

	x_{13}	x_{14}	x_{15}	x_{16}	x_{17}	x_{18}	x_{19}	x_{20}	x_{21}	x_{22}	x_{23}	x_{24}	x_{25}	x_{26}	x_{27}	x_{28}	x_{29}
1	0	1	2	0	1	2	0	2	1	19	9	2	1	1990	2655	2950	3650
2	0	1	2	0	1	2	0	2	1	19	9	2	1	1990	2655	2950	3650
3	1	1	2	0	1	2	0	1	1	19	19	3	19	2350	2550	2660	3650
4	1	1	2	0	1	2	0	2	2	19	19	2	1	2350	2655	2950	3650
5	1	1	2	0	3	2	0	2	9	3	1	3	1	2350	2550	2660	3650
6	0	1	2	0	0	0	0	8	12	2	19	1	1	2350	2770	3485	3650
7	0	1	2	0	0	0	0	8	1	3	1	3	1	2350	2550	2660	3650
8	0	1	2	0	1	2	0	2	1	2	9	2	1	2350	2655	2950	3650
9	0	1	2	0	0	0	0	8	1	19	9	2	10	1990	2330	2880	3650
10	0	1	2	0	0	0	0	8	1	19	9	2	10	1990	2330	2880	3650
11	0	1	2	0	1	2	0	2	2	19	9	2	1	1990	2655	2830	3650
12	0	1	2	0	0	0	0	2	12	10	9	2	1	2350	2655	2950	3650
13	0	1	2	0	0	0	0	2	12	10	9	2	1	2350	2655	2950	3650
14	**1**	**1**	**2**	**0**	**0**	**0**	**0**	**2**	**12**	**10**	**19**	**3**	**1**	**2350**	**2770**	**3485**	**3650**
15	1	1	2	0	0	0	0	2	20	10	9	2	1	2350	2655	2950	3650
16	1	0	2	4	2	5	0	2	20	11	19	2	7	2350	2655	2950	3650
17	1	0	2	0	2	2	0	8	20	19	19	2	1	2350	2655	2950	3650
18	1	0	2	4	2	2	0	2	20	19	9	2	1	2350	2655	2950	3650
19	1	0	2	4	2	2	0	2	20	19	19	2	1	2350	2655	2950	3650
20	**3**	**4**	**3**	**4**	**1**	**2**	**0**	**2**	**20**	**20**	**16**	**11**	**1**	**2350**	**2550**	**2950**	**3650**

List of Figure Captions

Figure 1. The Whiffle tree rig applies the total load to the blade at eight locations distributed along its length.

Figure 2. (a) Locations of the load bars and their proportion of the total load and (b) the bending moment distribution over the blade for a 1 kN load applied by the crane.

Figure 3. Layups for the three main regions of the blade and ply drop locations for the blade optimisation procedure.

Figure 4. The finite element model of the blade indicating the loads and boundary conditions.

Figure 5. Mesh convergence study for the GFPP blade.

Figure 6. Schematic of the two-point crossover procedure.

Figure 7. Comparison of experimental and FE blade mass values.

Figure 8. Locations of the centres of gravity of the GFPP and CFPP blades (a) along the length of the blades and (b) in the chord-wise direction.

Figure 9. Blade deflection results from the experiments and FE models for the GFPP, CFPP and optimum blades.

Figure 10. Comparison of the tip deflection results from the experiments and FE models (normalised by blade length).

Figure 11. Point cloud results from the laser scans during testing. The unloaded and loaded blade scans are overlaid.

Figure 12. The first three bending mode natural frequencies of the blades from the modal tests and FE models.

Figure 13. Comparison between experimental results and FE models of the strain in the two blades.

Figure 14. Strain results at several load levels in the CFPP blade.
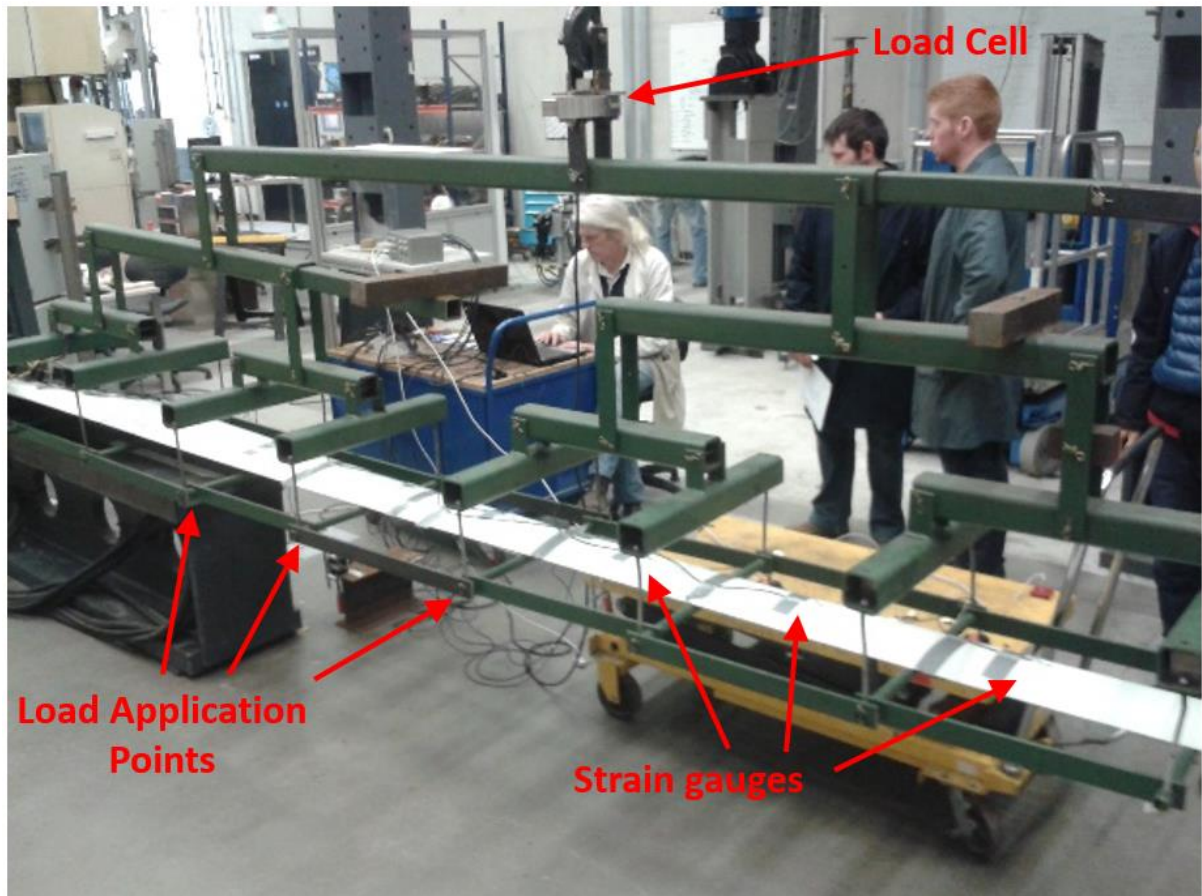
Figure 1
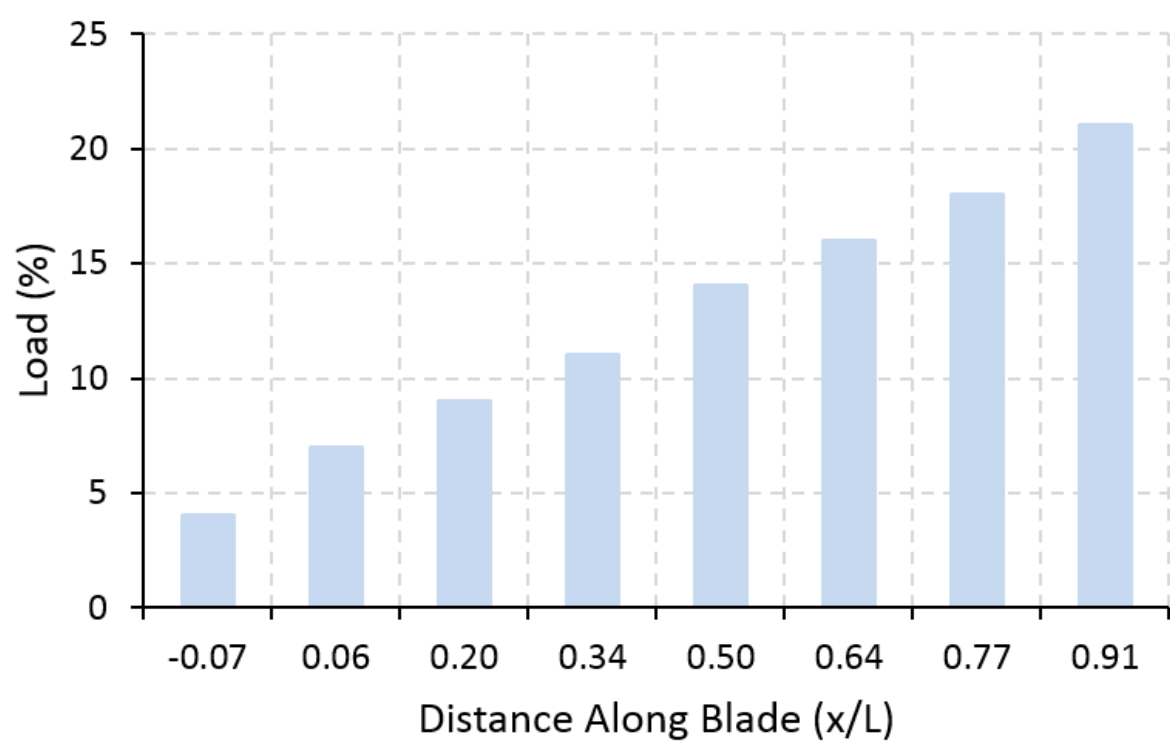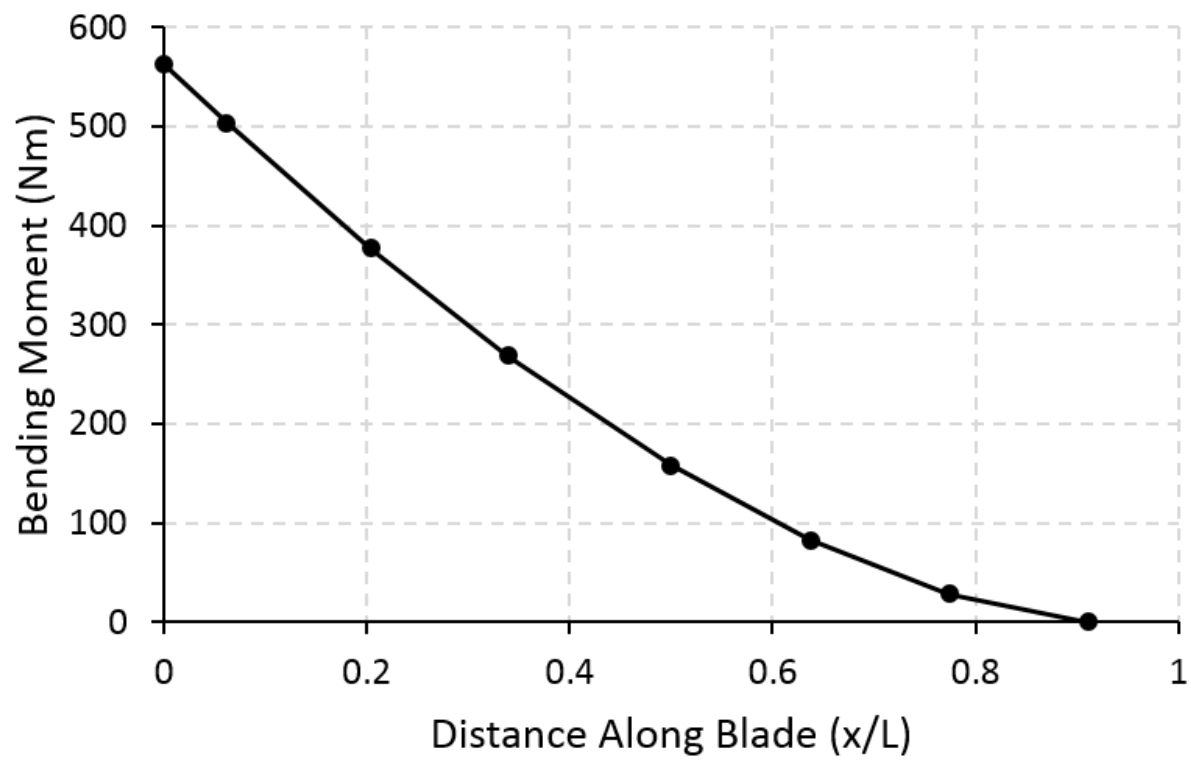
Figure 2 (a)

Figure 2 (b)
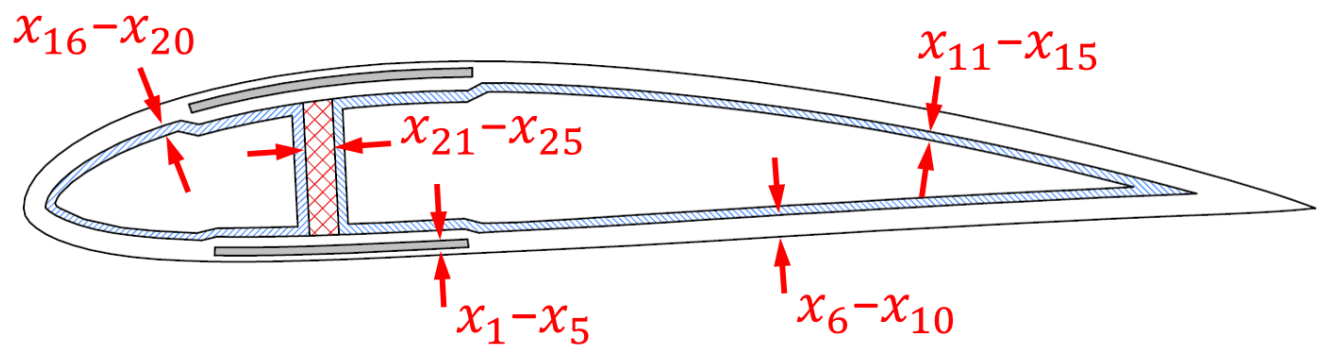
Figure 3 (a)
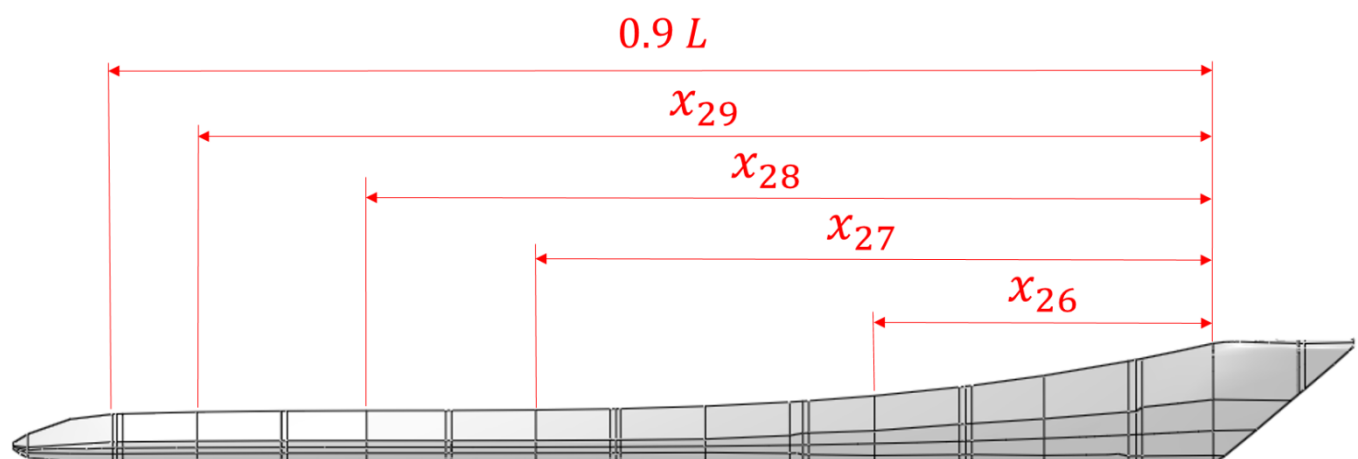
Figure 3 (b)

Figure 4

Figure 5

Split Points

Two unique parents p_1 and p_2

Resulting in either c_1, c_2 or c_3
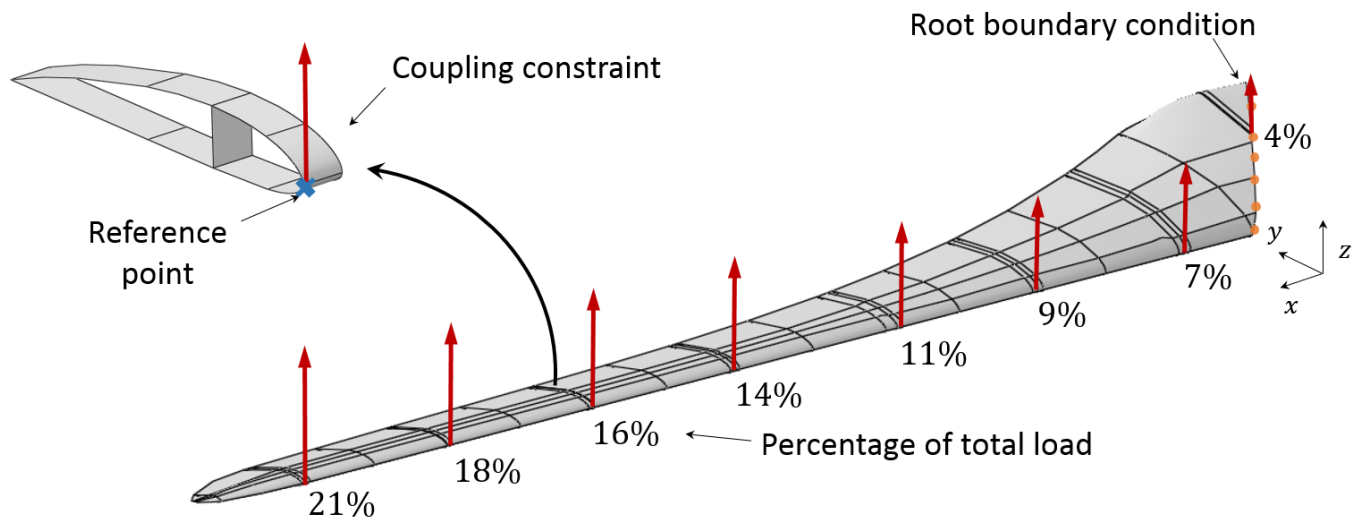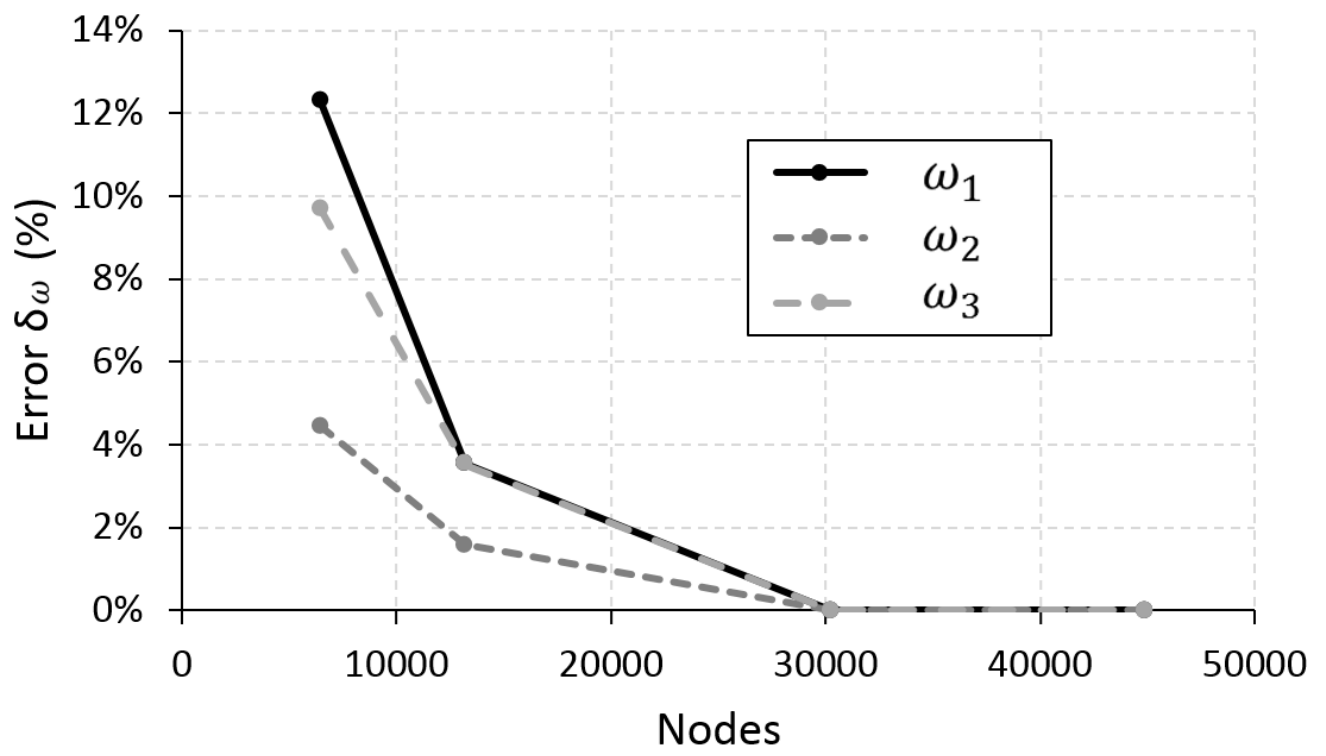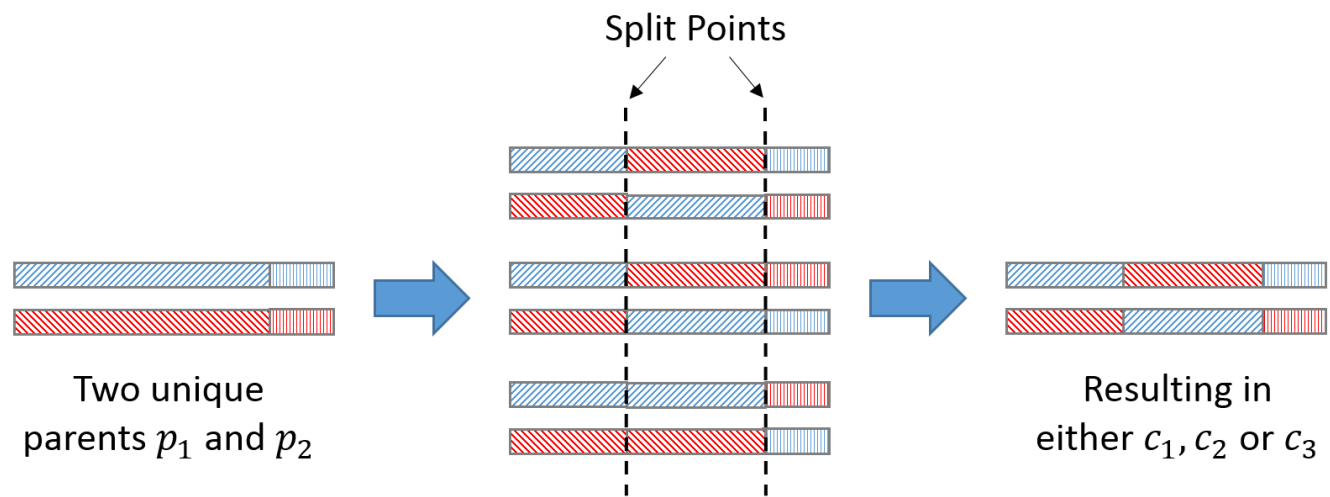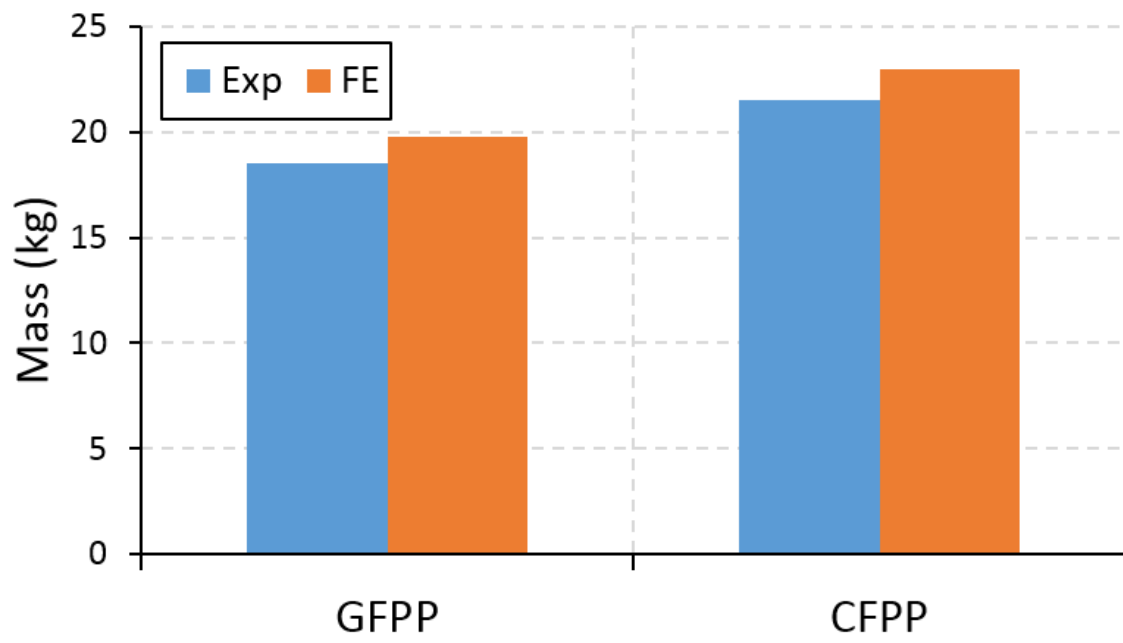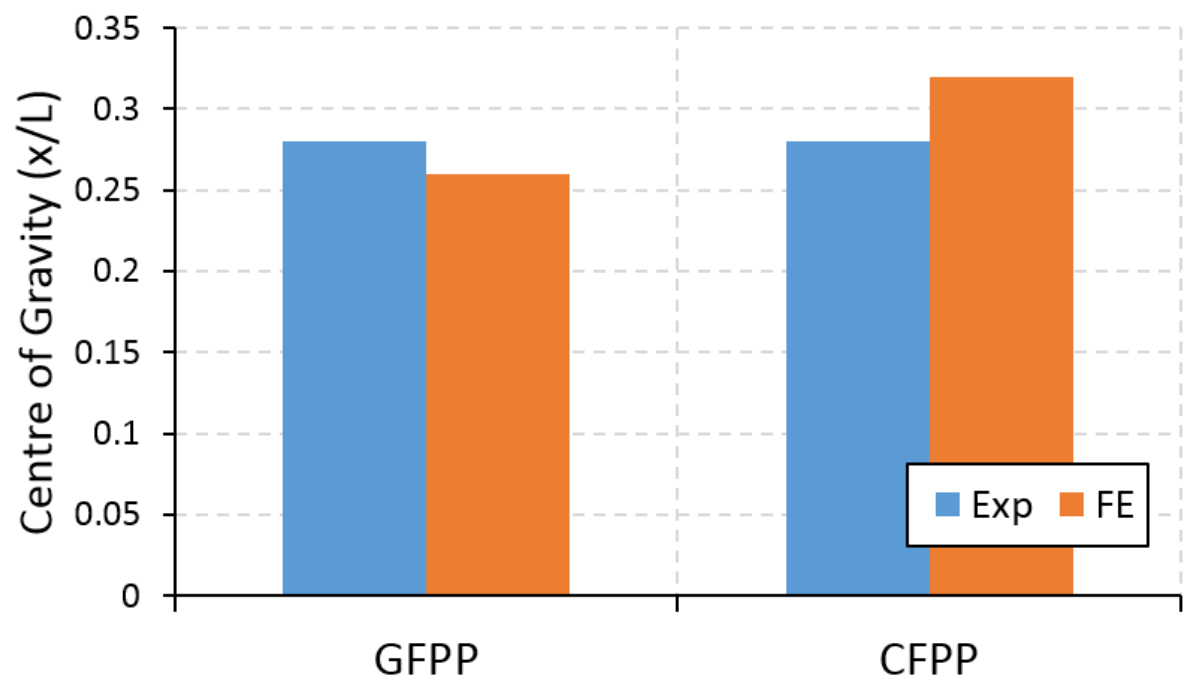
Figure 6

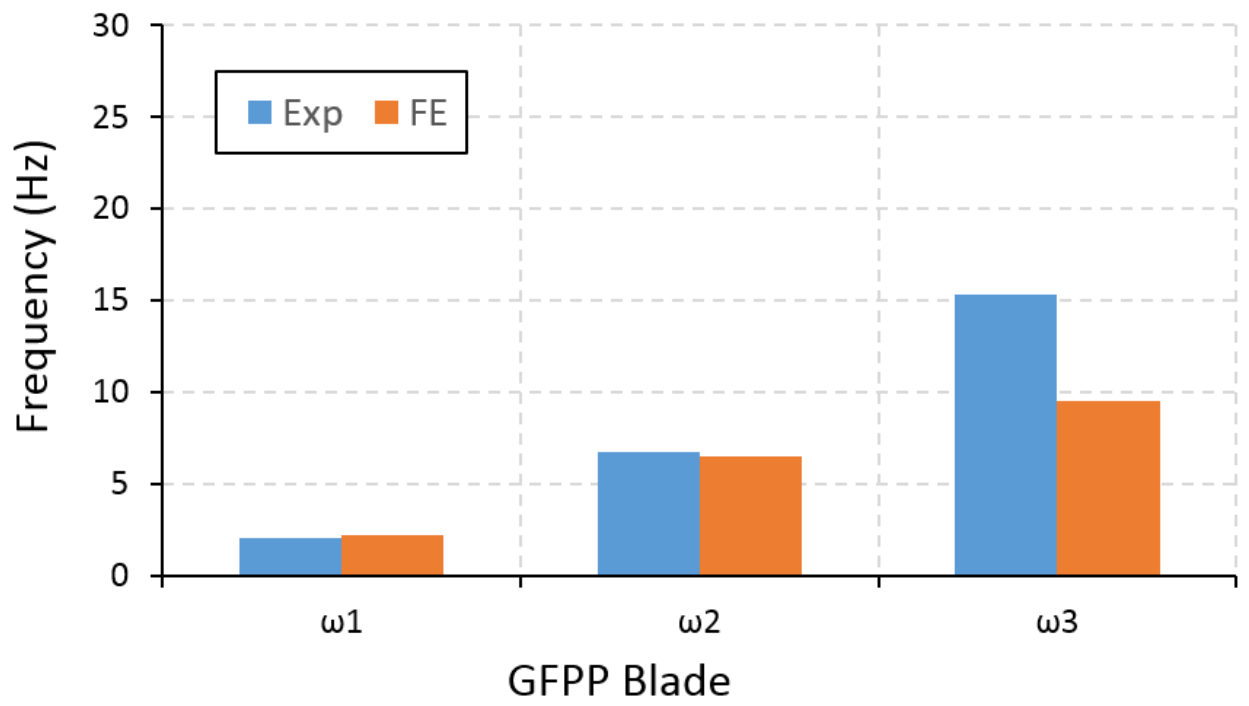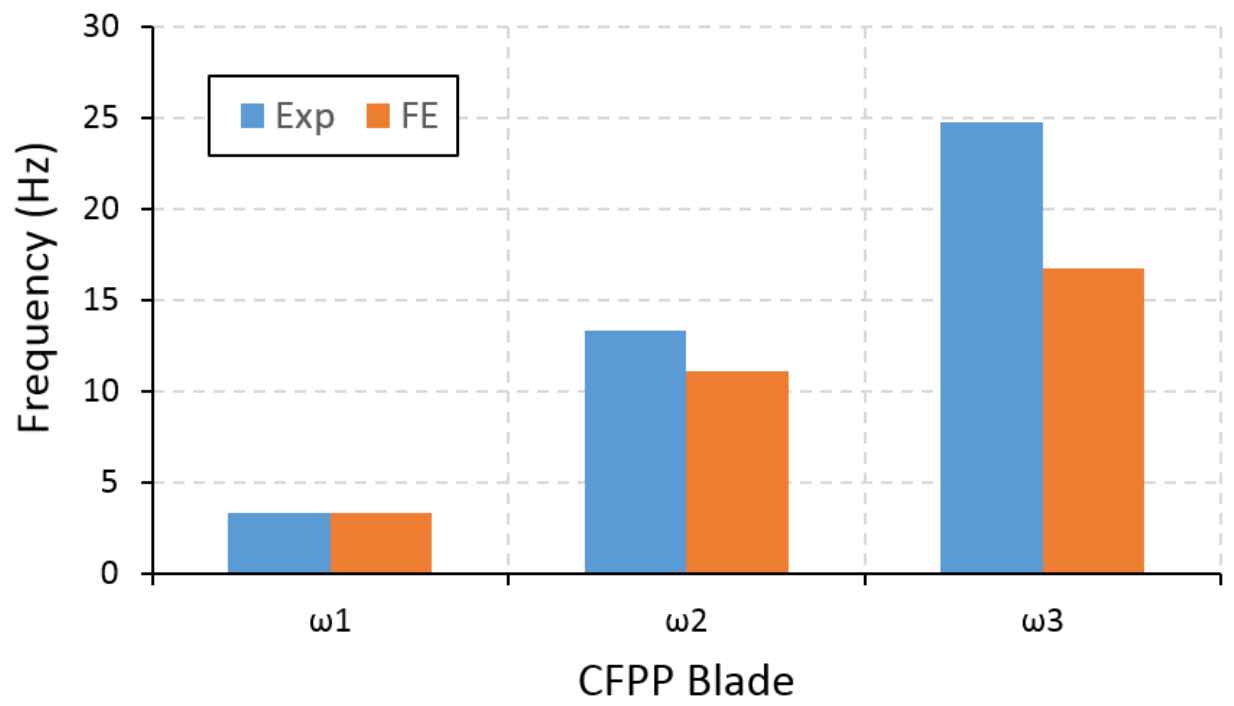Figure 7

Figure 8 (a)
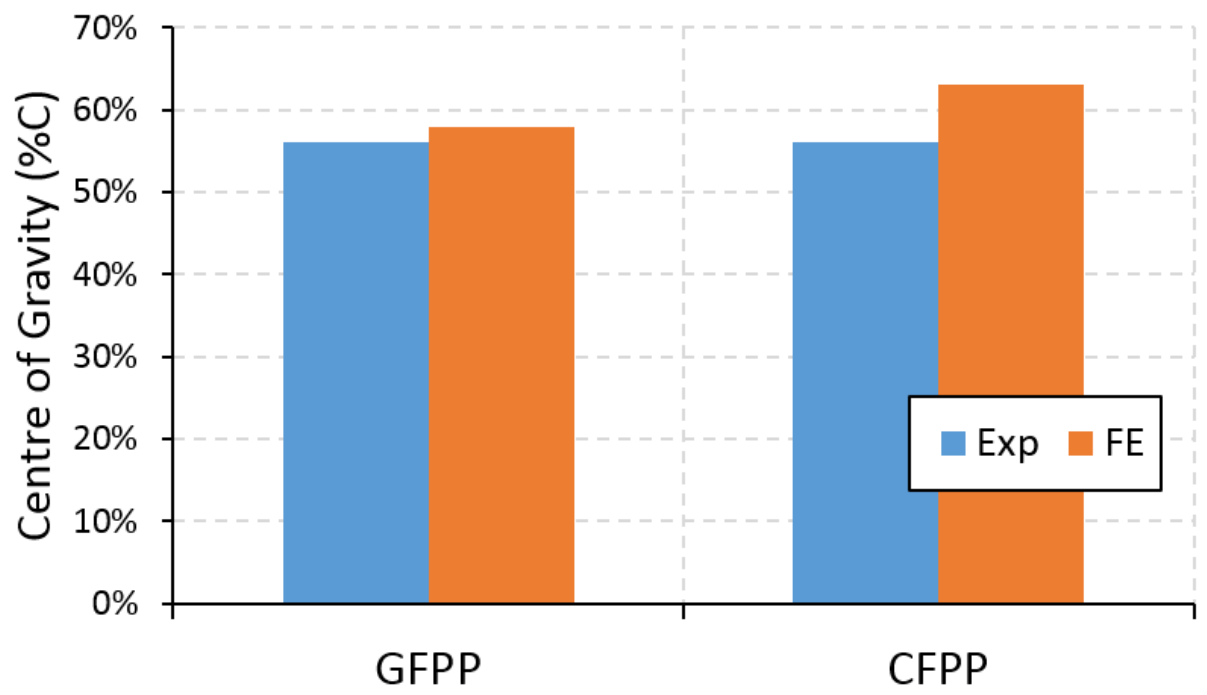
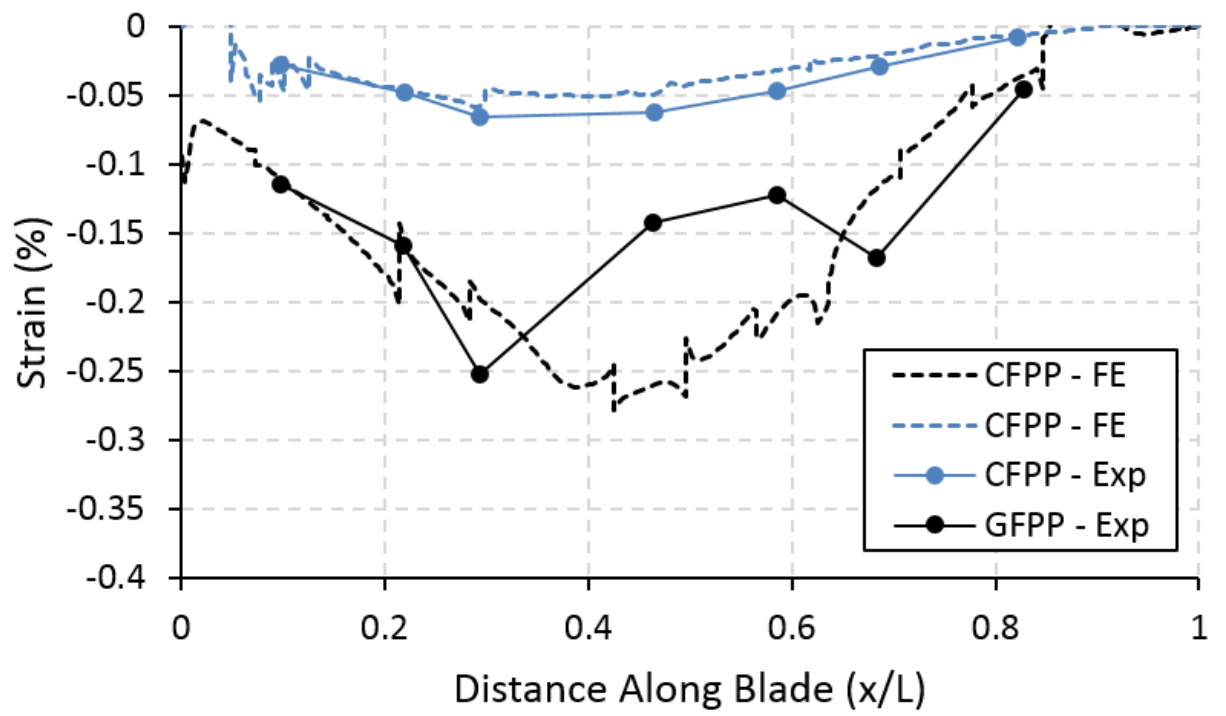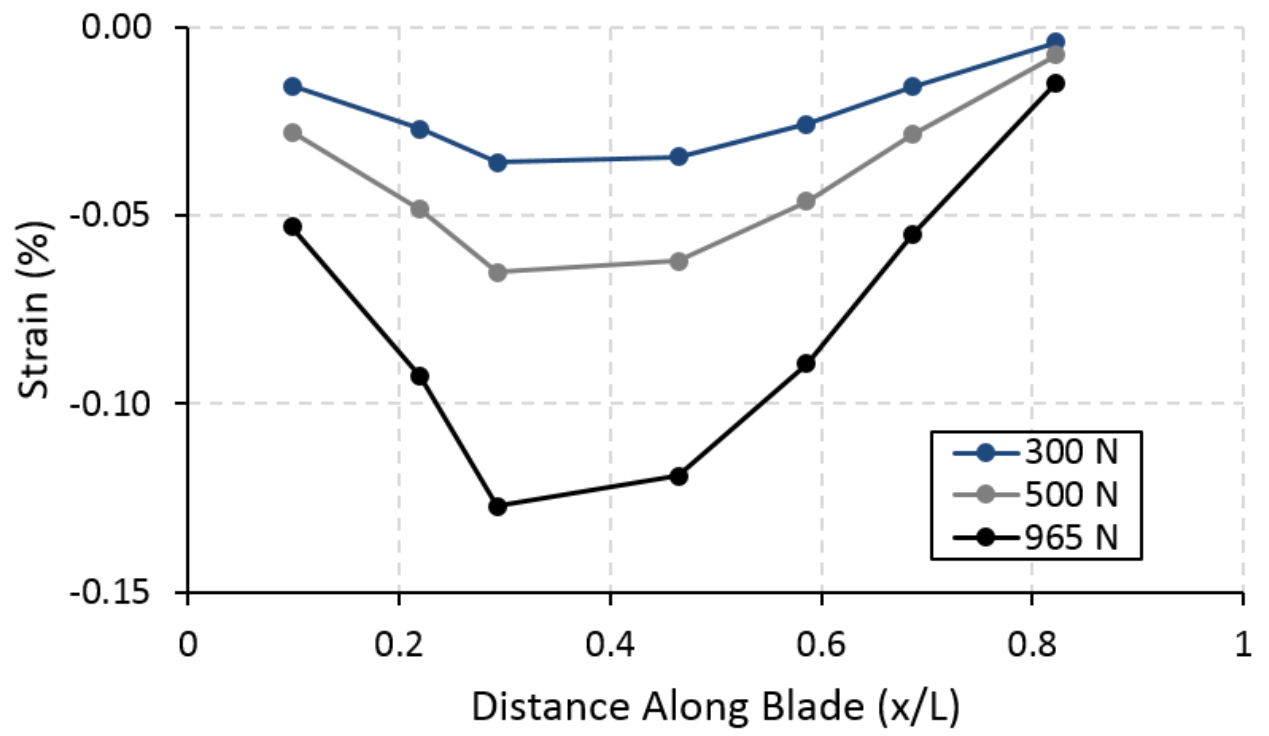Figure 8 (b)
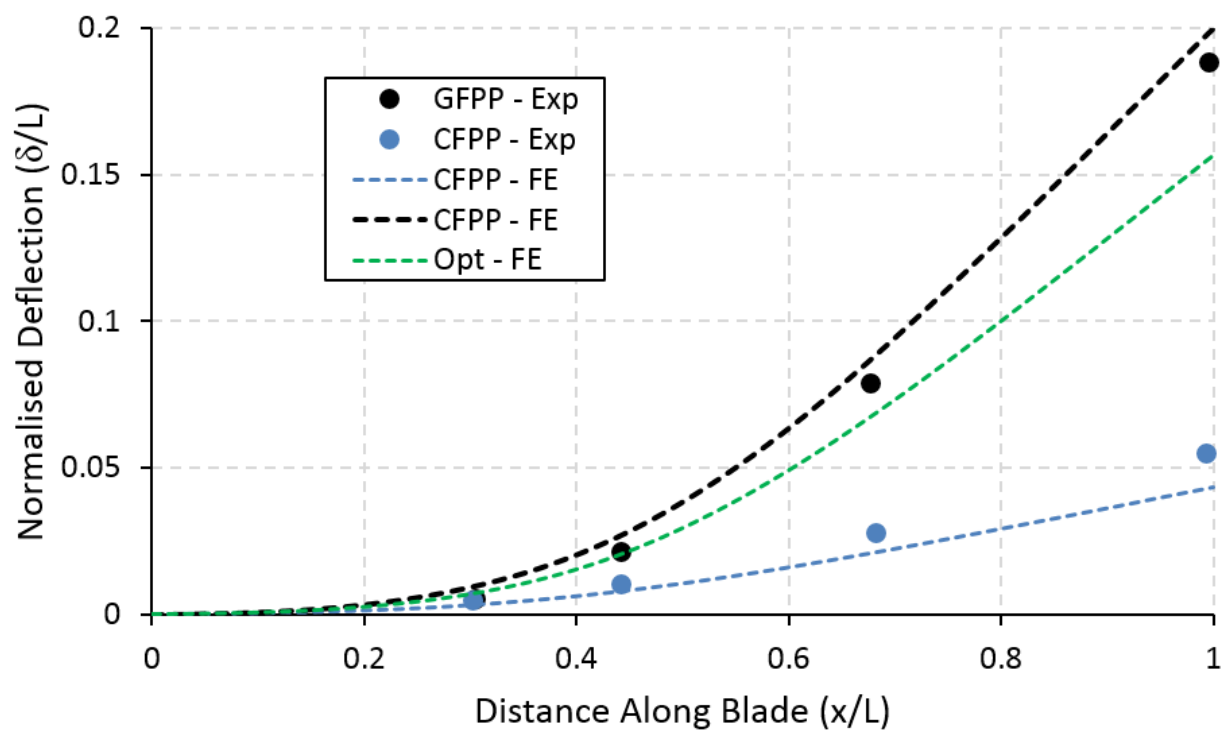
Figure 9
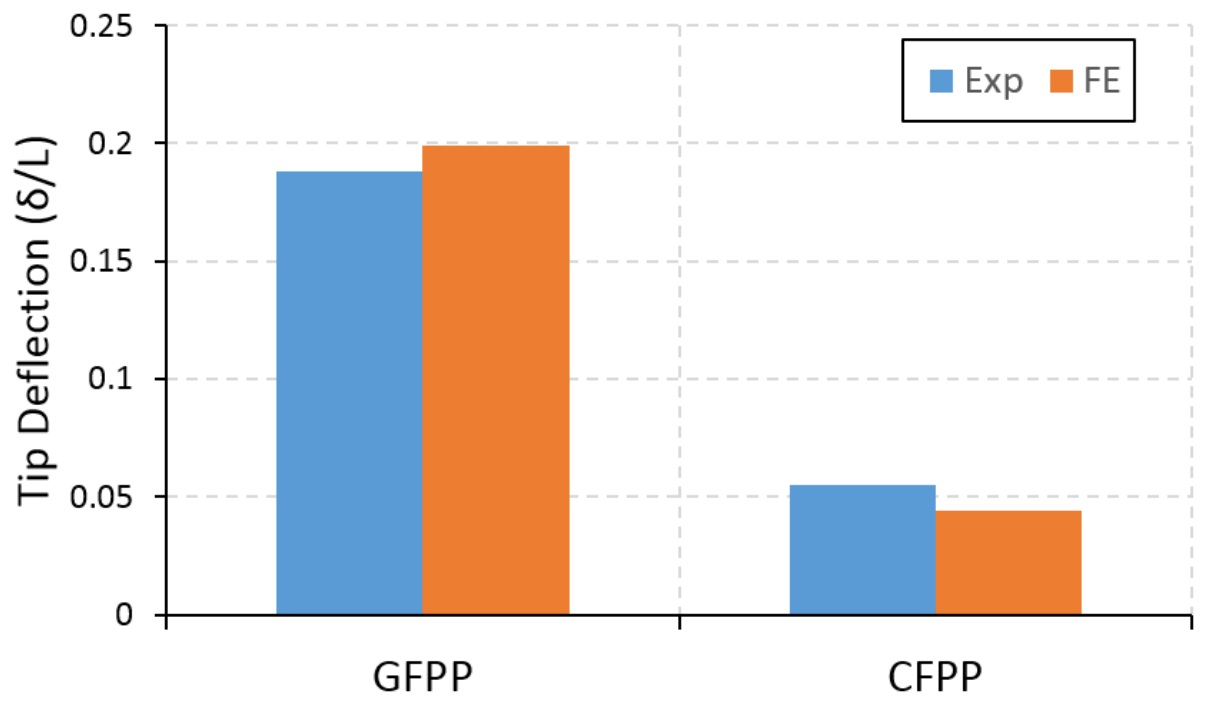
Figure 10

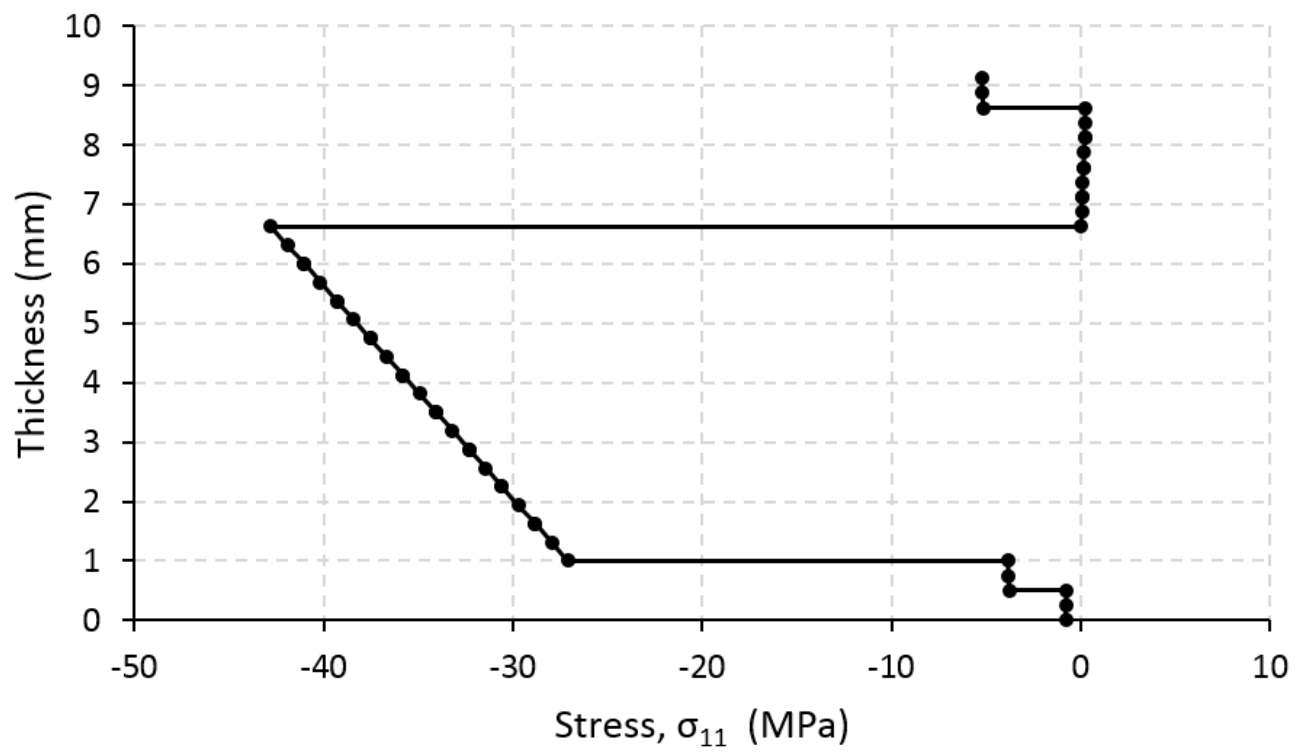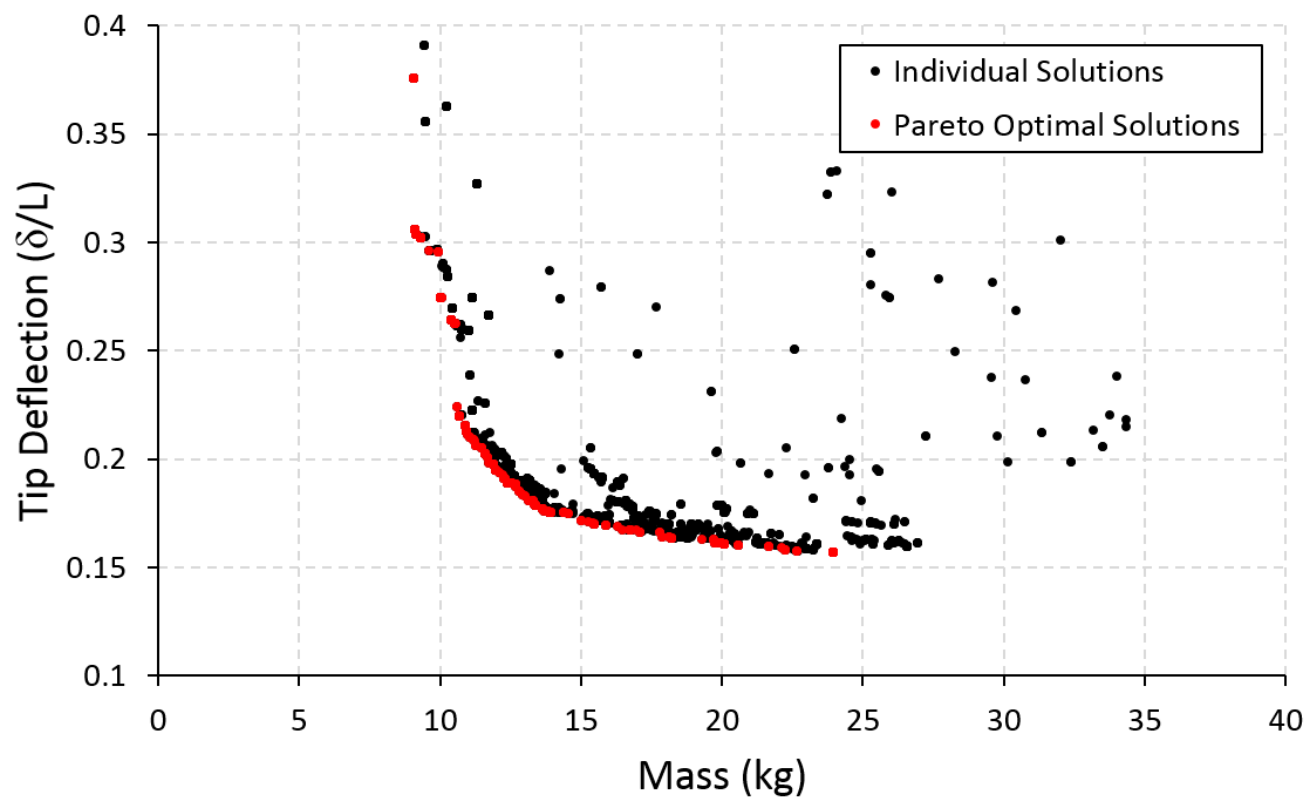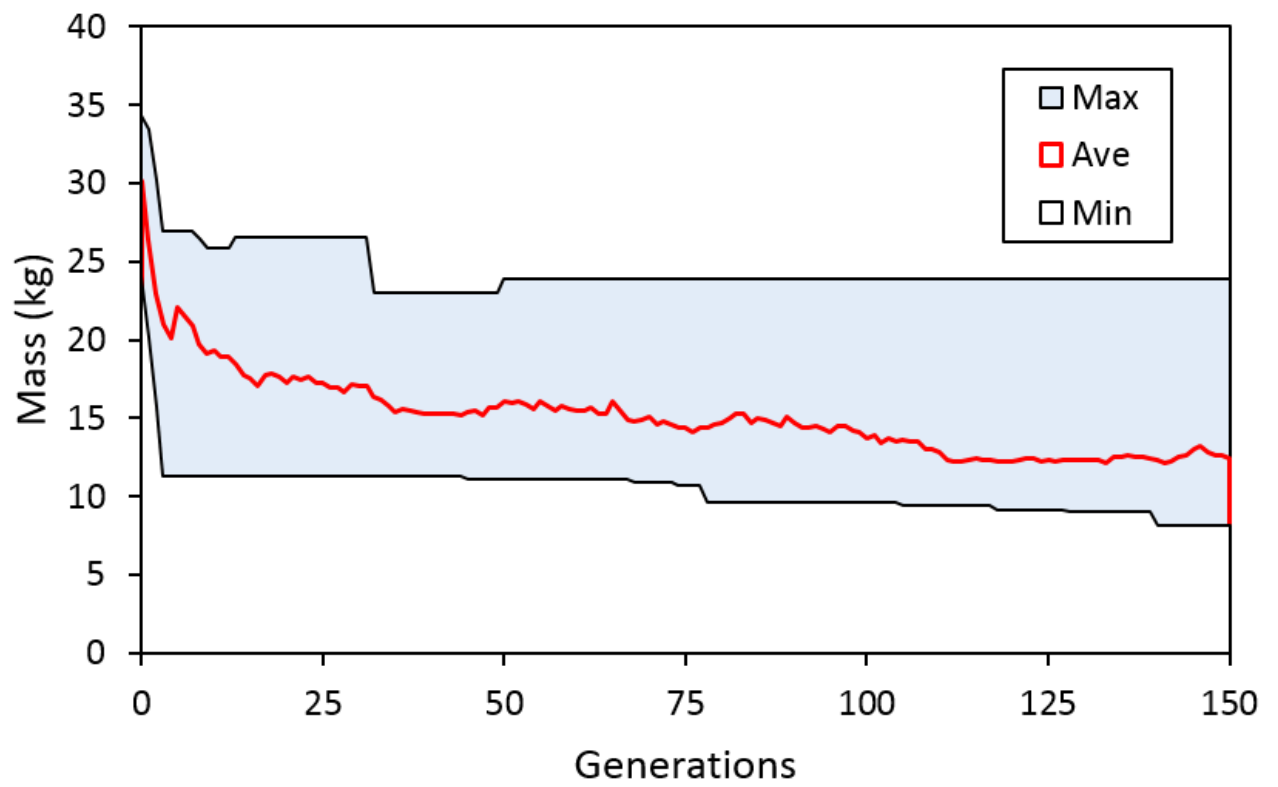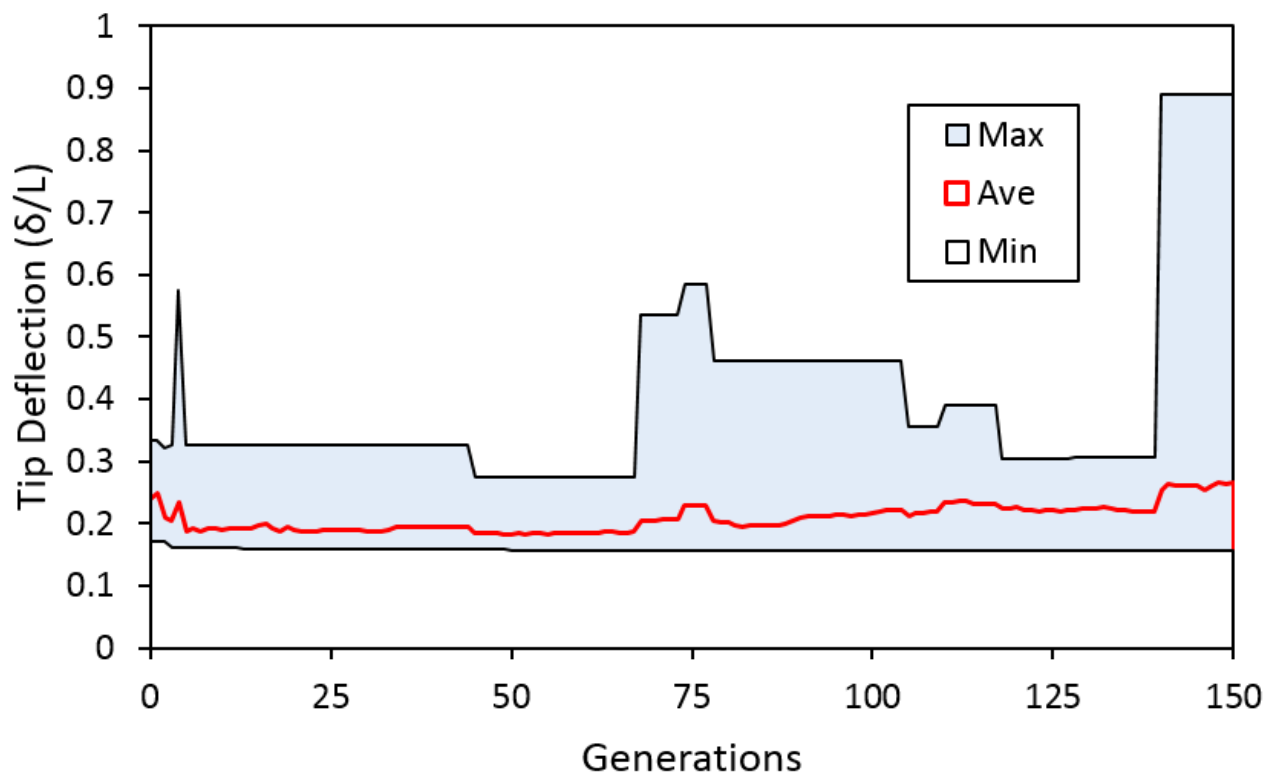Figure 11

Figure 12 (a)

Figure 12 (b)

Figure 13

Figure 14

Figure 15

Figure 16

Figure 17 (a)

Figure 17 (b)

Figure 18

Figure 19